ACS APPLIED MATERIALS & INTERFACES

Research Article

Cite This: ACS Appl. Mater. Interfaces 2018, 10, 28909−28917

www.acsami.org

Generating Sub-nanometer Pores in Single-Layer MoS_2 by Heavy-Ion Bombardment for Gas Separation: A Theoretical Perspective

Kedi Yin,[†,‡] Shengxi Huang,[§,∥] Xiaofei Chen,[†] Xinwei Wang,[⊥] Jing Kong,[*,§] Yan Chen,[*,‡] and Jianming Xue[*,†]

[†]State Key Laboratory of Nuclear Physics and Technology, School of Physics, CAPT, HEDPS, and IFSA Collaborative Innovation Center of MoE, Peking University, Beijing 100871, China

[‡]Guangzhou Key Laboratory for Surface Chemistry of Energy Materials, New Energy Research Institute, School of Environment and Energy, South China University of Technology, Guangzhou, Guangdong 510006, China

[§]Department of Electrical Engineering and Computer Science, Massachusetts Institute of Technology, Cambridge, Massachusetts 02139, United States

[∥]Department of Electrical Engineering, The Pennsylvania State University, University Park, Pennsylvania 16802, United States

[⊥]School of Advanced Materials, Shenzhen Graduate School, Peking University, Shenzhen 518055, China

Supporting Information

ABSTRACT: Single-layer molybdenum disulfide (MoS_2) filters with nanometer-size pores have attracted great attention recently due to their promising performance for membrane separation. Generating nanopores in MoS_2 controllably, however, is still a challenging task, which greatly limits the real application of MoS_2 filters. In this work, the pore forming process in single-layer MoS_2 by heavy-ion bombardment was investigated in detail using molecular dynamics simulations. We found that pores with sub-nanometer size (0.6−1.2 nm) can be created in the MoS_2 sheet by single-ion bombardment, with a probability as high as 0.8 pores per incident ion. The size and shape of the nanopore can be tuned controllably by adjusting bombardment parameters. Furthermore, the performance of the MoS_2 filter with these sub-nanometer-size pores for separation of He, Ne, H_2, Ar, and Kr gases was evaluated by density functional theory-based first-principles calculations. The MoS_2 filter was found to show much higher selectivity for separating H_2/He and He/Ne than that reported for graphene and other membranes. Such high selectivity was attributed to the interaction between gases and the charged edge of pores in MoS_2. Our results suggest the potential application of ion beam technology in single-layer MoS_2 for membrane separation.

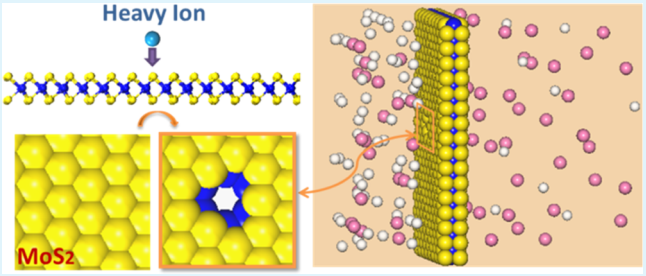

KEYWORDS: *single-layer MoS_2, molecular dynamic, density function theory, ion beam bombardment, nanopore, gas separation*

1. INTRODUCTION

Due to its potentially low cost, environmentally friendly, and high-efficiency features, two-dimensional (2D) materials with nanopores have attracted great attention in membrane separation technology,[1,2] such as gas separation,[2−5] water desalination,[6−8] and DNA sequencing.[9−11] Until now, graphene is the most widely studied 2D material for these applications.[5,7,12−16] In addition to graphene, single-layer MoS_2 with nanosize pores recently has also become a promising candidate.[8,10,17] For instance, Heiranian et al. predicted a nanopore in single-layer MoS_2 to have good performance for water desalination with water flux that is orders of magnitude greater than that of other known nanoporous membranes.[8] By introducing mechanical strain, Li et al. observed the "open" and "closed" states of the MoS_2 filter for water desalination in their simulations, pointing possible application as tunable nanodevices.[17] Farimani et al. reported that a single-layer MoS_2 showed much higher signal-to-noise ratio for DNA sequencing than graphene and boron nitride.[10] These superb performances of the MoS_2 filter were attributed to the craftable pore architecture (pore size and pore edge atoms) of MoS_2. Furthermore, in contrast to the charge-neutral edge of pores in graphene,[14] the edge of nanopores in the MoS_2 filter is intrinsically charged, which can also potentially play an essential role in achieving high efficiency.[17]

Generating pores with nanometer size in a controllable manner is essential for achieving membrane separation devices with high efficiency.[1,2,18,19] Many approaches have been applied to "drill pores" in graphene,[20−22] e.g., electron beam sculpting;[20] self-organized growth in high-temperature solvents, e.g., in zinc chloride;[21] and ultraviolet-induced oxidative etching.[22] The large-scale application of these approaches, however, is limited by their low efficiency, high cost, and the difficulty to control below 1 nm.[20] In contrast to these

Received: June 25, 2018
Accepted: July 31, 2018
Published: July 31, 2018

DOI: 10.1021/acsami.8b10569
ACS Appl. Mater. Interfaces 2018, 10, 28909−28917

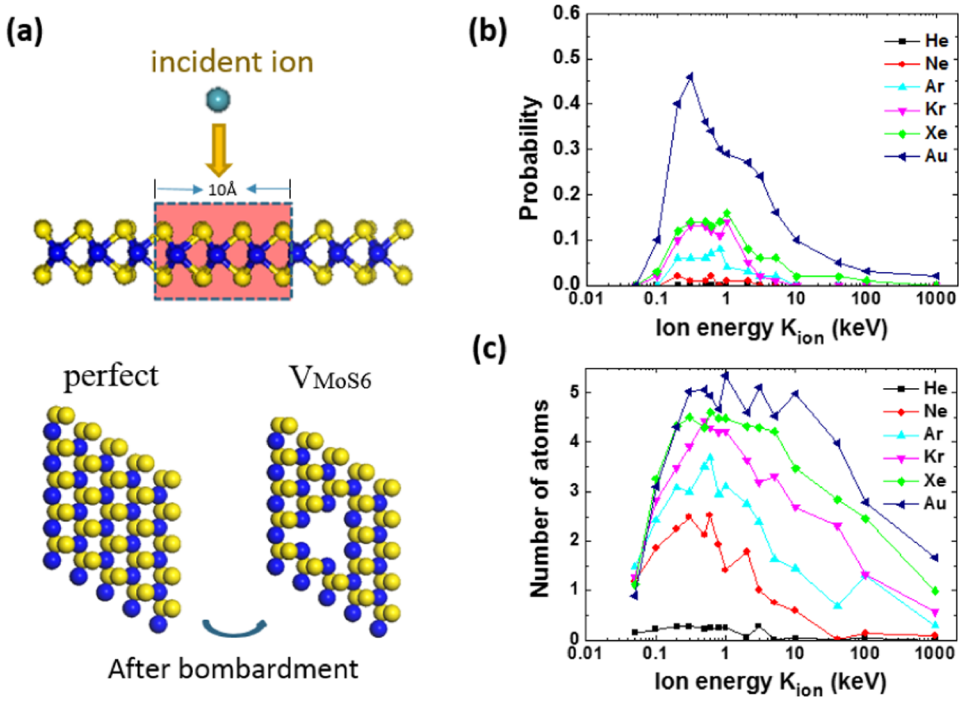

Figure 1. (a) Schematic presentation of the simulation setup, the perfect single-layer MoS_2, and the single-layer MoS_2 with a V_{MoS_6} nanopore (defect cluster) created by ion bombardment. (b) Probability of the production of nanopore (V_{MoS_6}). (c) Average number of sputtered atoms in single-layer MoS_2 under ion bombardment as a function of ion energy for the six types of ions revealed by MD simulations.

methods, it is still a challenging task to form nanopores controllably in single-layer MoS_2, which strongly limits its real application in membrane separation techniques.

Utilizing irradiation effects of energetic heavy ions in materials, ion beam technology has been successfully applied to engineer the structure and other properties of nanomaterials.[23−28] Our previous molecular simulation works showed that, by controlling the bombardment parameters (energies, species, incident angles, etc.), nanopores with expected size, shape, and quality could be created in graphene.[27,29,30] Such prediction was confirmed experimentally by Vázquez et al.[30] Furthermore, ion bombardment can also introduce reactive defects into the graphene lattice, which can be subsequently enlarged into permeable pores by oxidative etching.[31] All of these successful applications demonstrate ion beam bombardment to be a highly effective and economical way to fabricate nanopores in graphene and can be potentially applied to other two-dimensional materials. Although some previous works have studied the radiation effect of heavy ions in single-layer MoS_2,[32−36] the creation of nanopores in single-layer MoS_2 by ion irradiation has not been systematically explored yet.

In this work, we employed molecular dynamic (MD) simulations to investigate the formation of nanopores in single-layer MoS_2 by ion bombardment. MD simulation has been widely used in describing the interaction between heavy ions and two-dimensional materials.[23−26,37,38] Our group previously used MD simulations to investigate the doping and defect-generating process of energetic ions in graphene.[25,26] The defect-production probability predicted by MD simulation was then found to agree well with experimental values.[26] In this article, we found that pores with sub-nanometer size (0.6−1.2 nm) in a MoS_2 sheet can be created by single-ion bombardment. The probability to produce sub-nanometer pores in single-layer MoS_2 can be as high as 0.8 by selecting appropriate ion parameters. The pore shape and pore size can be tuned controllably by adjusting the ion mass, energy, and incident angle. To demonstrate the application of the MoS_2 filter with sub-nanometer-size pores created by heavy-ion bombardment, we further used density functional theory (DFT)-based first-principles calculations to evaluate its performance for gas separation. The transportation of He, Ne, H_2, Ar, and Kr through sub-nanometer pores introduced by ion bombardment was studied in detail. We found that the nanopores in single-layer MoS_2 showed very high selectivity and permeability for separating H_2/He and He/Ne, much higher than that reported for graphene and other membranes. Such high selectivity was attributed to the charge of the pore in MoS_2. Our results pointed out the potential application of ion beam technology in MoS_2 and other two-dimensional materials for membrane separation applications.

2. THEORETICAL CALCULATIONS

2.1. MD Simulation. Molecular dynamics simulations were performed on the large-scale/molecular massively parallel simulator.[39] The Stillinger−Weber potential recently developed by Jiang's group was used to describe the interatomic interactions within single-layer MoS_2 for stable molecular dynamics simulations.[40,41] To model the energetic collisions between incident ions with single-layer MoS_2, the Ziegler−Biersack−Littmark (ZBL)[42,43] universal repulsive potential, which can accurately describe the interaction at short interatomic separations (<1 Å), was used. Except for the noble incident ions, the Au−S interatomic interactions were also calculated with only the ZBL potential, which is based on the fact that the binding energy of Au−S is very weak compared to that of Mo−Mo, S−Mo, and S−S.

Ion irradiation was conducted on a free-standing MoS_2 sheet consisting of 576 Mo atoms and 1152 S atoms, with a lateral

DOI: 10.1021/acsami.8b10569
ACS Appl. Mater. Interfaces 2018, 10, 28909−28917

size of 65 × 75 Å^2. Periodic boundary conditions were used during the dynamical simulations. He, Ne, Ar, Kr, Xe, and Au ions were chosen to simulate the ion impacts. The incident ion was initially placed at 20 Å above the single-layer MoS_2, and the direction was perpendicular to the MoS_2 sheet. Ion energies were in the range of 50 eV to 1000 keV. For Au ions, the incident angle was taken from 0° (normal direction with respect to the surface) to 60°. For each incident ion with a specific energy, 100 independent simulations were carried out, and the impact points were randomly distributed in a 10 × 10 Å^2 square area located in the sample center so as to simulate as much impact points as possible. During the irradiation process, the NVE ensemble was employed and a time step of 0.1 fs was used to guarantee energy conservation. After the collision, the system was maintained at 300 K for 50 ps with the Nosé–Hoover algorithm.

2.2. DFT Simulation. The first-principles calculations were carried out based on the spin-polarized DFT[44] as implemented in the Vienna ab initio simulation package (VASP).[45,46] The electron–ion interaction was described by the projector augmented wave[47,48] pseudopotentials. The exchange and correlation potentials were described by the generalized gradient approximation[49] functional of Perdew–Burke–Ernzerhof (PBE).[49] To account for the influence of the van der Waals[50] interaction, the optPBE method was used, as in our previous works.[51,52] All calculations were performed with a supercell of single-layer MoS_2 containing 108 atoms. The periodic boundary condition was applied, and a vacuum layer of 15 Å was added to avoid the interlayer interactions. The total energy was converged to better than 10 meV for a plane wave cutoff of 500 eV and 5 × 5 × 1 Monkhorst–Pack[53] *k*-point sampling for the Brillouin zone. For geometry relaxation, we used the method of conjugate gradient energy minimization, and the convergence criterion for energy was 10^{-5} eV between two consecutive steps. The maximal force exerted on each atom was less than 0.02 eV/Å upon ionic relaxation.

To explore the performance of this sub-nanometer pore in gas separation, the climbing image nudged elastic band (CI-NEB) method[54] was performed to estimate the diffusion barrier for gases transporting through the pore. Hereby, the starting and the end positions of the molecular diffusion pathway are placed above and below the central pore, whereas a linear interpolation between those points was used as an initial guess of the diffusion path. Ab initio molecular dynamics (ab init MD) simulation was also carried out to check the thermal stability of the nanoporous MoS_2. The configuration from the static calculation was used as the initial state, and a canonical NVT ensemble was simulated using the algorithm of Nosé. The system was allowed to relax for 15 ps in total with a time step of 3 fs.

3. RESULTS AND DISCUSSION

When energetic ions bombard a single-layer MoS_2, as illustrated in Figure 1a, Mo or S atoms can obtain enough energy to escape from the single-layer MoS_2, resulting in different defect structures in MoS_2. In our simulations, six types of ions (He, Ne, Ar, Kr, Xe, and Au ions) with energies ranging from 50 eV to 1000 keV were used as incident ions. The incident direction was set to be perpendicular to the MoS_2 plane. We found that, for all of these conditions, a vacancy complex containing a Mo vacancy and nearby three disulfur pair vacancies ((V_{MoS_6}) can be formed after ion bombardment (Figure 1a). This V_{MoS_6} defect cluster is treated as a nanopore with an effective diameter of 0.6 nm, which can potentially be used in membrane separation applications. As for S vacancy, Mo vacancy, and some other complex point defects, even if they are produced, they would not affect the separation application of the pore due to their small effective diameters. The formation process of the V_{MoS_6} defect cluster can be described as follows: first, the S atoms in the upper sublayer, which directly interact with the incident ion, will be sputtered away in the opposite direction of the incident ion; the knock-on Mo atom will then become the new energetic ion to hit the S atoms in the lower sublayer downward, which finally lead to the formation of the V_{MoS_6} defect cluster.

The dependence of the pore formation process on the kinetic energy of ions was investigated in detail. The nanopore-production probability shows a volcano shape dependence on the kinetic energy of incident ions (Figure 1b). For a given ion, as the kinetic energy increases from 50 eV to 1000 keV, the possibility to create a nanopore first increases with ion kinetic energy and then decreases. The reason for such volcano shape dependence is that the formation of nanopore is mainly derived from atomic sputtering. As shown in Figure 1c, the number of sputtered atoms caused by energetic ion bombardment shows a very similar dependence on the kinetic energy of incident ions, indicating atomic sputtering to be the main cause of nanopore formation. It is worth noting that, besides being sputtered away from the MoS_2 surface, some target atoms may leave their original position but still be attached to the MoS_2 plane, which can also contribute to the formation of nanopores. We did not count this part into the average number of sputtered atoms. For the energy regime studied in this work, the number of sputtered atoms is mainly dominated by the energy transferred between the incident ion and the atom,[32] which is positively correlated to the collision cross section. The initial increase of nanopore-production probability with ion energy is because low-energy ions simply cannot displace target atoms. However, the decrease of nanopore-production probability originates from a drop in the cross section at high ion energies.[55−58] The ion kinetic energy that shows the maximum probability to form a V_{MoS_6} pore is in the range of hundreds to thousands of electron volts for all of the six types of incident ions.

The ion mass also has a significant impact on the nanopore forming process (Figure 1b). At a given ion energy, a heavier ion shows a greater probability to create V_{MoS_6} pores in single-layer MoS_2. Consistent with the high pore-production probability, single-layer MoS_2 bombarded by heavier ions shows a larger number of sputtered atoms (Figure 1c), and our results in Figure 1c for He, Ne, Ar, Kr, and Xe are consistent with early theoretical studies of single-layer MoS_2 subjected to ion irradiation.[32] Furthermore, as shown Figure 1b, the probability shows a more pronounced dependence on the kinetic energy for heavier ions. This is similar to the dependence of nuclear stopping power (S_n), defined as the energy transferred to the target atoms per unit distance, on the mass of incident ion. However, the definition of nuclear stopping power is based on averaging over many collisions, which is not useful for a two-dimensional material.[27] The S_n values of the six types of ions with different energies in bulk MoS_2 calculated by the stopping and range of ions in matter[59] software are shown in Figure S1. The mass and energy

DOI: 10.1021/acsami.8b10569
ACS Appl. Mater. Interfaces 2018, 10, 28909−28917

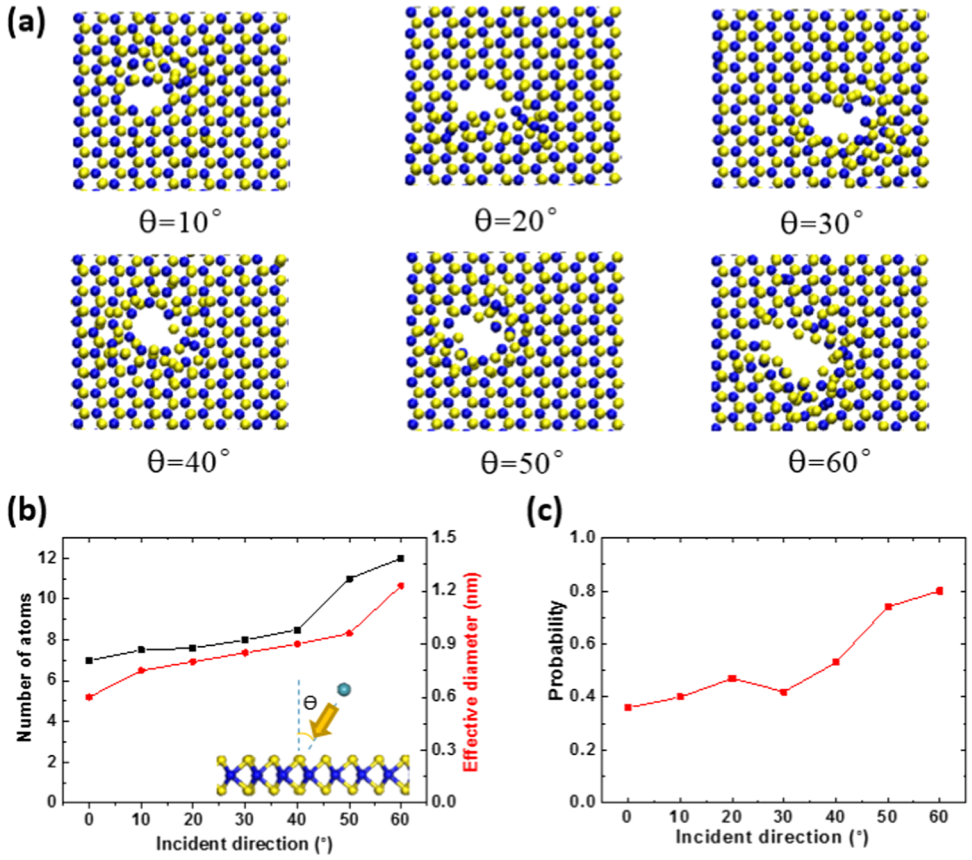

Figure 2. Influence of the ion incident angle on the pore forming process. (a) Final atomic configurations resulted from the incidence of 500 eV Au atom with different incident angles. (b) Average number of removed atoms and the effective diameter of pores created by 500 eV Au bombardment with different incident angles. (c) Probability to form pores as a function of incident angle for 500 eV Au ion bombardment.

dependence tendency shown in Figure 1b is also widely observed in other applications of ion beam when sputtering is involved.[24,27,29] It is worth noting that besides V_{MoS_6} other defect types can also be formed in the ion bombardment, as shown in Figure S2. The dependence of the formation probabilities for some different defects (V_S, V_{S_2}, V_{Mo}, V_{MoS_3}, V_{MoS_5}, V_{MoS_6}, and pores larger than V_{MoS_6}) on the kinetic energy for Au ion irradiation is shown in Figure S3.

Besides the mass and the kinetic energy, the incident angle of the heavy-ion can also strongly impact the interaction of energetic ions and 2D material. For instance, it has been reported that an increased incident angle can cause more severe damage in graphene.[27,60] Therefore, it could be expected that more atoms can be removed and a larger pore could be produced when larger incident angles were used. To study the impact of the incident angle, 500 eV Au ions were chosen as the injection ions in the following simulation due to their high possibility to create nanopores (Figure 1b,c). We keep the simulation size in the oblique incidence, and the incident angle (θ) was taken from 0 to 60°. Figure 2a shows pores with various nanostructures formed by ion bombardment at different incident angles. In contrast to the above-mentioned V_{MoS_6} nanopore that shows a regular round shape, nanopores formed by ions with large incident angles usually have complex structures featuring very rough edges. As the incident angle increases, the generated nanopores become less circular and increasingly elliptical. Because we are considering the random impact points, the effective diameter, which is defined as an imaginary cylinder coaxial with the thread has equal space widths, was used to characterize these pores. Characterization of pore geometry by the effective diameter is shown in Supporting Information S-4. The effective diameters of the nanopores range from 0.6 to 1.2 nm as the incident angle increases from 0 to 60° (Figure 2b). This phenomenon is due to the impact of incident angle on the energy transfer process between the incident ions and the target atoms. When the incident angle increases, more energy will be deposited into the MoS_2 sheet because of the longer interaction path between the incident ion and the MoS_2 layer, which will lead to more severe damage and eventually bigger nanopores in single-layer MoS_2.

We also calculated the pore-production probability as a function of ion incident angle, as shown in Figure 2c. With the increase in incident angle, the probability to form nanopores keeps increasing except for a little drop around 30°. This drop is because the minimum energy for atoms to escape also depends on the escape angle. For example, if there is another atom in the way of the sputtered atom, excess energy is needed to overcome this new barrier, resulting in the dropping of the sputtering efficiency.[27,61] One thing worth mentioning is that the probability to form a nanopore can be as high as 80% for 60° incident angle.

Among all of the ions used in our simulation, Au has the largest mass and highest efficiency to drill pores in the MoS_2 sheet. For example, the probability of a 300 eV Au ion with vertical incident angle to create a nanopore is as high as 0.48 pore/ion. The ion flux for the irradiation beam experiment is

DOI: 10.1021/acsami.8b10569
ACS Appl. Mater. Interfaces 2018, 10, 28909−28917

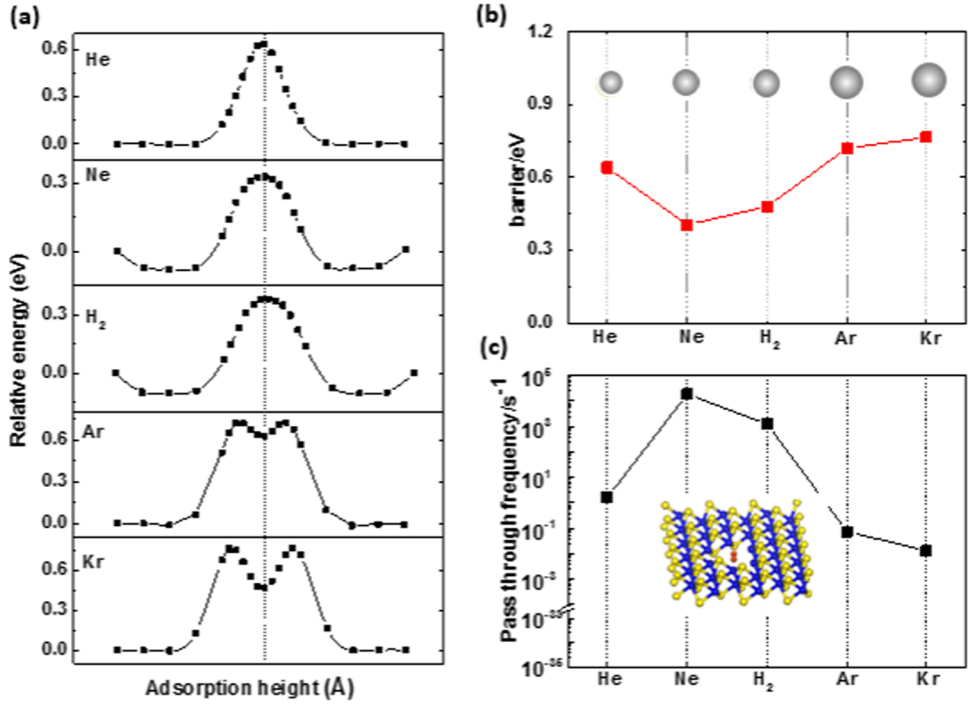

Figure 3. (a) Change of the relative energy as a function of gas adsorption height as it passes through the pore. The dashed line shows the position of the MoS_2 plane. (b) Calculated diffusion barriers (red squares) of different molecular species. The diffusion barrier for a given gas to pass through the MoS_2 filter is defined to be the energy difference between the maximum energy and the minimum energy along the migration path. The size of the ball represents the kinetic diameter of different gases, which increases from left to right. (c) Pass-through frequencies for different gases. The inset shows the transition state of the hydrogen molecule.

usually at least 10^{10} cm^{-2}/s. This means billions of sub-nanometer pores can be produced per second by Au ion bombardment, indicating the ion beam technique to be an efficient approach to generate sub-nanometer pores in single-layer MoS_2. One thing worth noting is that when one pore is created, the probability to form other pores next to it is very low. On the one hand, the ion flux of 10^{10} cm^{-2}/s in an experiment means that only one ion will incident onto the 10 nm × 10 nm area of the MoS_2 sheet per second, indicating a very low probability of pore overlapping. On the other hand, it is very easy to bombard any sample in a way that the sample is irradiated homogenously, e.g., by scanning. It is also worth noting that, in the nuclear stopping regime, the Au ion can produce nanopores in the MoS_2 sheet with very high efficiency, whereas it is difficult to do so in graphene.[55,62] This is because more than one collisions happen in single-layer MoS_2 as an analogy to the cascade collision in a bulk system, which can introduce great damage in the target materials by incident ions, with a much higher probability compared with that in graphene. When the incident ions knock out one target atom in the MoS_2 sample, this first knock-on atom may collide with other atoms in the MoS_2 sample, thus causing more atoms to be removed from the MoS_2 sample. In this case, complex defects, such as the nanopores we observed, can even be produced by a single-ion bombardment. However, for graphene, damage often exists in the initial incident ion collisions and secondary collision caused by the first knock-on atoms could hardly occur.

Among the nanopores generated by heavy-ion bombardment shown above, the V_{MoS_6} nanopore is the most promising for the application in membrane separation.[17] On the one hand, the V_{MoS_6} pore has a regular and stable pore edge, whereas the larger pores we get show relatively poor stability and the smaller pores have too small effective diameters and poor stability to pass through the gases. To show the thermodynamic stabilities of the V_{MoS_6} pore, V_{MoS_5} pore, and the larger pore (e.g., $V_{Mo_3S_{16}}$), we explore the configuration change before and after the 25 ps relaxation at room temperature (300 K), as shown in Figures S4–S6. We found that the deformation of the V_{MoS_6} pore is only 3%, indicating that the V_{MoS_6} pore structure remains stable at room temperature. However, the atomic configuration of V_{MoS_5} and the larger pore changed continuously over time, indicating their poor stability. On the other hand, the diameter of V_{MoS_6} pore is about 0.6 nm, which is comparable to the size of gases. It has been reported that a sub-nanometer pore is a fundamental prerequisite to achieving good selectivity for gas separation.[1,19,63] To evaluate the performance of the MoS_2 filter obtained by ion irradiation for gas separation, the DFT calculation was applied to determine the selectivity of several gases (He, Ne, H_2, Ar, and Kr).

First, the diffusion barriers for different gases (He, Ne, H_2, Ar, and Kr) were calculated using the climbing image nudged elastic band (CI-NEB) scheme. The starting and ending positions of the molecular diffusion pathway were placed above and below the center of the nanopore. A linear interpolation between the starting and ending points was used as an initial guess of the diffusion path.[19] Twenty intermediate images were created by interpolating between the initial and final states, which are chosen as the local minimum configurations obtained in the relaxation runs. It is worth noting that H_2 passing through the nanopore in the vertical direction has the lowest diffusion barrier, as well as the highest priority.

DOI: 10.1021/acsami.8b10569
ACS Appl. Mater. Interfaces 2018, 10, 28909−28917

Table 1. Calculated Selectivities at Room Temperature for Different Molecular Combinations Assuming a Prefactor of 10^{11} s^{-1} for All Species

structure	He	Ne	H_2	Ar	Kr
He		1.1×10^{4}	7.3×10^{2}	2.2×10^{1}	1.3×10^{2}
Ne	9.1×10^{-5}		1.5×10^{1}	2.5×10^{5}	1.4×10^{6}
H_2	1.4×10^{-3}	6.6×10^{-2}		1.6×10^{4}	9.2×10^{4}
Ar	4.5×10^{-2}	4.1×10^{-6}	6.1×10^{-5}		5.7×10^{0}
Kr	7.9×10^{-3}	7.2×10^{-7}	1.1×10^{-5}	1.8×10^{-1}	

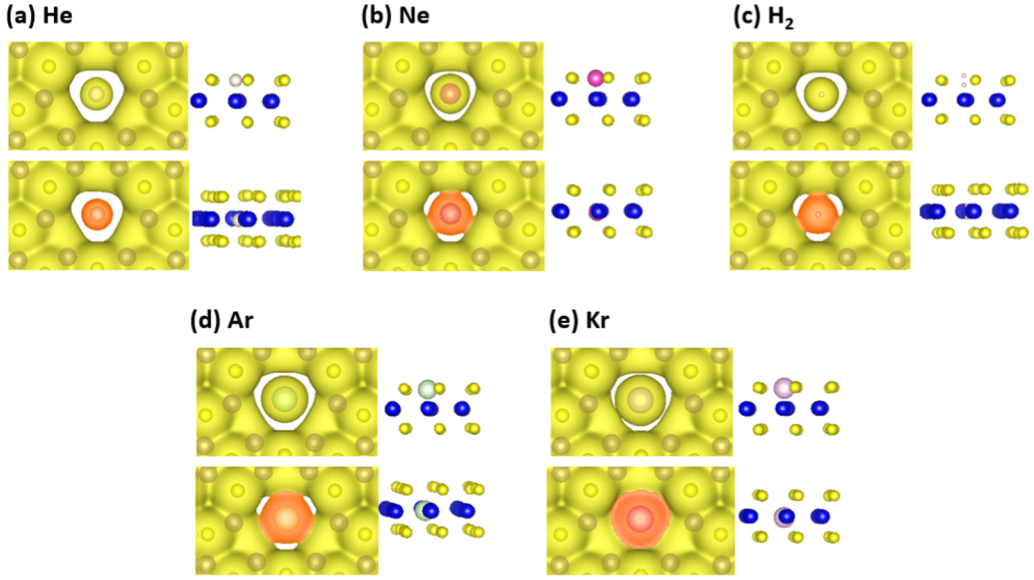

Figure 4. Charge densities of different gases and nanopores during the penetration process are represented by yellow and brown surfaces for a better comparison. The isosurface value is 0.01 e/Å^3 for both yellow and brown surfaces. (a) He; (b) Ne; (c) H_2; (d) Ar; and (e) Kr. The energy minimum point at the upper layer of the MoS_2 sheet and the middle of the pore in MoS_2 sheet have been chosen to calculate the charge density for He, Ne, and H_2. The maximum point and the minimum point in the valley-shaped curves have been chosen to calculate the charge densities for Ar and Kr. There is clear deformation of the charge density toward the passing H_2, He, Ne, Ar, and Kr when they get close to the MoS_2 sheet.

Therefore, we did the calculation only for the case when H_2 vertically passes through the nanopore, as reported in many other literature works.[1,18,19] By setting the energy of the initial configuration to be 0, the energy of other intermediate states relative to the initial configuration can be obtained (Figure 3a). The diffusion barrier for a given gas to pass through the MoS_2 filter is then defined to be the energy difference between the maximum energy and the minimum energy, as shown in Figure 3b.

The so-called kinetic diameter, defined by the molecular distance at the minimum of the Lennard-Jones potential for nonpolar molecules and the Stockmayer potential for polar molecules,[64] has been widely used for describing the transport mechanism of molecules through membranes with micropores.[65] The kinetic diameters of He, Ne, H_2, Ar, and Kr are 0.26,[66] 0.275,[67] 0.289,[66] 0.34,[67] and 0.36 nm,[67] respectively. However, our results demonstrate that the kinetic diameter does not correlate well with the diffusion barrier of the gas, as shown in Figure 3b. For instance, Ne has a bigger kinetic diameter than He but shows a smaller diffusion barrier (0.4 eV) than He (0.64 eV). Similar inverted orders can also be found for H_2/He (0.47 and 0.64 eV for H_2 and He, respectively). The interaction between gases and the charged edge of the MoS_2 nanopore is the reason why the kinetic diameter is not applicable to our case, which will be discussed later.

The selectivity (selectivity = $A^X/A^Y = \exp(-(\Delta E_X - \Delta E_Y)/k_BT)$ between species X and Y) was estimated using diffusion barriers ΔE and the Arrhenius equation $A = A_0 \exp(-\Delta E/k_BT)$, where A is the diffusion rate (pass-through frequency), A_0 is the diffusion prefactor, k_B is the Boltzmann constant, and T is the temperature.[19] The estimated selectivities for different molecular combinations at room temperature are listed in Table 1. We find that the single-layer MoS_2 with the V_{MoS_6} pore has selectivity of nearly 10^3 for H_2/He separation, which is nearly 2 order of magnitude higher than that of nanoporous graphene (around 10)[19] and other microporous membranes such as metal, silica, polymer, etc. (less than 10).[54] Moreover, the selectivity for the most frequent studies of He/Ne separation (>10^4) is also much higher than that for porous silica-based ultimate membranes, polyphenylene, and porous graphene (several hundreds to several thousands).[19,63] Furthermore, the MoS_2 filter exhibits a high selectivity for Ne from other larger noble gases (selectivity > 10^5) due to the exceptionally low diffusion barrier.

The pass-through frequency (the number of times that gases pass through the nanopore per second) for all gases was also estimated using the same prefactor $A_0 = 10^{11}$ s^{-1} as in other reports.[19,63] We found that the diffusion barriers of Ne and H_2 can be overcome quite frequently. In contrast to larger gases Ar and Kr that exhibit significantly low pass-through frequencies (<0.1 s^{-1}), Ne and H_2 exhibit a very high pass-through frequency, with 10^4 and 10^3 s^{-1} for Ne and H_2, respectively.

DOI: 10.1021/acsami.8b10569
ACS Appl. Mater. Interfaces 2018, 10, 28909−28917

The pass-through frequency for Ne (10^4 s^{-1}) here is much higher than for Ne through graphene nanopores (1 s^{-1}).[19] The pass-through frequency of He (2 s^{-1}) also allows a good separation of this species from larger gases.

Both the selectivity and pass-through frequency results indicate that the MoS_2 filter with V_{MoS_6} nanopores shows great potential for practical application in gas separation. As shown in the previous section, the difference in the diffusion barrier for different gases cannot be explained by their kinetic diameter. The charged edge of a nanopore in the MoS_2 sheet was reported to alter the ion selectivity and water permeability.[17] Chemical functional groups such as hydroxyl groups bonded to the edges of graphene pores were also found to roughly double the water flux due to their hydrophilic character.[14] Therefore, it is very likely that the charged edge of the sub-nanometer pores in the MoS_2 sheet also strongly impacts the penetration process of the gas.

It has been shown that charge distribution can be strongly localized around the defects in single-layer MoS_2.[68−70] To understand the charge transfer between the gas atom and the monolayer during the gas penetration process, we calculate the effective charge on individual atom. Here, we present a comprehensive study on the properties of various charge states based on the Bader analysis[71] and the first-principles calculation.[45] Using the VASP code, the core charge and partition electrons among fragments of the system were quantified. Our results showed that He, Ne, H_2, Ar, and Kr lose 0.0594, 0.1184, 0.089, 0.115, and 0.0981 electrons to the MoS_2 sheet, respectively. Furthermore, we explore the charge density changes of the nanopores and the propagating gases during the penetration process. For Ar and Kr, the maximum point and the minimum point in the valley-shaped curves have been chosen to calculate the charge density (Figure 3a). For other gases, the energy minimum point at the upper layer of the MoS_2 sheet and the middle of the pore in the MoS_2 sheet have been chosen to calculate the charge densities, which are represented by yellow and brown isosurfaces, respectively, as shown in Figure 4. The charge densities were clearly deformed when H_2, Ne, Ar, and Kr were approaching the MoS_2 sheet, i.e., the isosurface level expanded toward the edge of the nanopores. This indicates that some attraction forces exist when the gas is close to the center of the pore. Combining the quantitative charge transfer calculated by Bader analysis and the qualitative charge density map shown in Figure 4, we found that Ne loses more electrons compared with He, which leads to a larger polarizability. Therefore, a stronger attractive electrostatic interaction will be formed between Ne and the MoS_2 sheet, as shown in Figure 4a,b. Such stronger electrostatic interaction leads to the lower energy barrier for Ne to pass through the nanopore compared to that for He, despite its larger kinetic diameter. A similar explanation can be applied to the comparison between H_2 and He. Furthermore, the valleylike shape at the top of the energy barrier for large gases, like Ar and Kr, can also be explained by the electrostatic interaction between gases and the nanopores (Figure 3a). As shown in Figure 4d,e, the charge density has a tendency to overlap with that of the surrounding atoms when the gas travels from the maximum point to the minimum point in the valley-shaped curve (Figure 3a).

It has been reported that the separation mechanism based on kinetic diameters becomes less applicable when attractive forces beyond van der Waals interactions occur.[18] Some previous studies also have validated the feasibility and rationality of this charge polarization mechanism based on the electrostatic interaction between the polarized gas and the charged edges.[17,19] Our results demonstrate that the unique characteristics of electron redistribution between Mo and S atoms at the nanopore edge of single-layer MoS_2 play an important role in determining the penetration process of gases, which are very likely to be the reason of the predicted high selectivity of the MoS_2 filter.

4. CONCLUSIONS

In this article, MD simulations have been carried out to investigate the pore forming process in single-layer MoS_2 by heavy-ion bombardment. Pores with sub-nanometer size (0.6−1.2 nm) in the MoS_2 sheet can be created by single-ion bombardment. In addition, the pore size and shape can be controlled by the ion parameters including mass, energy, and incident angle. Furthermore, we found that ions with kinetic energy in the range of 200 eV to 3 keV show the highest probability to create sub-nanometer pores in MoS_2. The probability to create sub-nanometer pores can be as high as 0.8 pores per incident ion, indicating that ion beam technology is a convenient and efficient way to create such pores in the MoS_2 sheet. We used DFT-based first-principles calculations to demonstrate the applicability of these sub-nanometer-size pores in MoS_2 for gas separation. The transport of He, Ne, H_2, Ar, and Kr through the V_{MoS_6} pore, which is one representative of the sub-nanometer pores formed by ion bombardment, was studied in detail. We found that the MoS_2 filter with V_{MoS_6} pores show high selectivity for separating H_2/He and He/Ne, which is orders of magnitude higher than that reported for graphene and other membranes. The high selectivity was attributed to the interaction between gases and the charge of the pore in MoS_2. Our results will guide the usage of ion beam technology in single-layer MoS_2 for membrane applications.

■ ASSOCIATED CONTENT

Supporting Information

The Supporting Information is available free of charge on the ACS Publications website at DOI: 10.1021/acsami.8b10569.

Nuclear stopping power (S_n) of the six ions with different energies in bulk MoS_2, intrinsic structural defects in single-layer MoS_2, dependence of the probability for different irradiation defects (V_S, V_{S_2}, V_{Mo}, V_{MoS_3}, V_{MoS_5}, V_{MoS_6}, and larger pores) on ion energy for Au ion irradiation, characterization of pore geometry by the effective diameter, the stability of the V_{MoS_6} pore at room temperature, the stability of the V_{MoS_5} pore and the larger pore (e.g., $V_{Mo_3S_{16}}$) at room temperature, the average number of sputtered atoms in single-layer MoS_2 under ion bombardment as a function of ion energy, the differential charge densities for all of the gases at the middle of the pore in the MoS_2 sheet (PDF)

■ AUTHOR INFORMATION

Corresponding Authors

*E-mail: jingkong@mit.edu (J.K.).
*E-mail: escheny@scut.edu.cn (Y.C.).
*E-mail: jmxue@pku.edu.cn (J.X.).

DOI: 10.1021/acsami.8b10569
ACS Appl. Mater. Interfaces 2018, 10, 28909−28917

ORCID

Xinwei Wang: 0000-0002-1191-8162
Jing Kong: 0000-0003-0551-1208
Yan Chen: 0000-0001-6193-7508

Notes

The authors declare no competing financial interest.

■ ACKNOWLEDGMENTS

This work was supported by the National Natural Science Foundation of China (No. 11605063), Guangdong Innovative and Entrepreneurial Research Team Program (No. 2014ZT05N200), Guangzhou Science and Technology Program General Projects (No. 201707010146), and the Recruitment Program of Global Youth Experts, IAEA (CRP No. F11020 and Contract No. 21063). J.K. acknowledges the support from the NSF Center for Energy Efficient Electronics Science (E3S).

■ REFERENCES

(1) Ambrosetti, A.; Silvestrelli, P. L. Gas Separation in Nanoporous Graphene from First Principle Calculations. *J. Phys. Chem. C* **2014**, *118*, 19172−19179.
(2) Li, D.; Hu, W.; Zhang, J.; Shi, H.; Chen, Q.; Sun, T.; Liang, L.; Wang, Q. Separation of Hydrogen Gas from Coal Gas by Graphene Nanopores. *J. Phys. Chem. C* **2015**, *119*, 25559−25565.
(3) Tsetseris, L.; Pantelides, S. T. Graphene: An impermeable or selectively permeable membrane for atomic species? *Carbon* **2014**, *67*, 58−63.
(4) Du, H.; Li, J.; Zhang, J.; Su, G.; Li, X.; Zhao, Y. Separation of Hydrogen and Nitrogen Gases with Porous Graphene Membrane. *J. Phys. Chem. C* **2011**, *115*, 23261−23266.
(5) Li, H.; Song, Z. N.; Zhang, X. J.; Huang, Y.; Li, S. G.; Mao, Y. T.; Ploehn, H. J.; Bao, Y.; Yu, M. Ultrathin, Molecular-Sieving Graphene Oxide Membranes for Selective Hydrogen Separation. *Science* **2013**, *342*, 95−98.
(6) Qiu, Y.-H.; Li, K.; Chen, W.-Y.; Si, W.; Tan, Q.-Y.; Chen, Y.-F. Ion and water transport in charge-modified graphene nanopores. *Chin. Phys. B* **2015**, *24*, No. 108201.
(7) Rollings, R. C.; Kuan, A. T.; Golovchenko, J. A. Ion selectivity of graphene nanopores. *Nat. Commun.* **2016**, *7*, No. 11408.
(8) Heiranian, M.; Farimani, A. B.; Aluru, N. R. Water desalination with a single-layer MoS_2 nanopore. *Nat. Commun.* **2015**, *6*, No. 8616.
(9) Liu, K.; Feng, J.; Kis, A.; Radenovic, A. Atomically thin molybdenum disulfide nanopores with high sensitivity for DNA translocation. *ACS Nano* **2014**, *8*, 2504.
(10) Farimani, A. B.; Min, K.; Aluru, N. R. DNA Base Detection Using a Single-Layer MoS_2. *ACS Nano* **2014**, *8*, 7914−7922.
(11) Feng, J.; Liu, K.; Bulushev, R. D.; Khlybov, S.; Dumcenco, D.; Kis, A.; Radenovic, A. Identification of single nucleotides in MoS_2 nanopores. *Nat. Nanotechnol.* **2015**, *10*, 1070−1076.
(12) Mishra, A. K.; Ramaprabhu, S. Functionalized graphene sheets for arsenic removal and desalination of sea water. *Desalination* **2011**, *282*, 39−45.
(13) Celebi, K.; Buchheim, J.; Wyss, R. M.; Droudian, A.; Gasser, P.; Shorubalko, I.; Kye, J. I.; Lee, C.; Park, H. G. Ultimate Permeation Across Atomically Thin Porous Graphene. *Science* **2014**, *344*, 289−292.
(14) Cohen-Tanugi, D.; Grossman, J. C. Water desalination across nanoporous graphene. *Nano Lett.* **2012**, *12*, 3602−3608.
(15) Shannon, M. A.; Bohn, P. W.; Elimelech, M.; Georgiadis, J. G.; Marinas, B. J.; Mayes, A. M. Science and technology for water purification in the coming decades. *Nature* **2008**, *452*, 301−310.
(16) Kim, H. W.; Yoon, H. W.; Yoon, S. M.; Yoo, B. M.; Ahn, B. K.; Cho, Y. H.; Shin, H. J.; Yang, H.; Paik, U.; Kwon, S.; Choi, J. Y.; Park, H. B. Selective Gas Transport Through Few-Layered Graphene and Graphene Oxide Membranes. *Science* **2013**, *342*, 91−95.
(17) Li, W.; Yang, Y.; Weber, J. K.; Zhang, G.; Zhou, R. Tunable, Strain-Controlled Nanoporous MoS_2 Filter for Water Desalination. *ACS Nano* **2016**, *10*, 1829−1835.
(18) Hauser, A. W.; Schwerdtfeger, P. Methane-selective nanoporous graphene membranes for gas purification. *Phys. Chem. Chem. Phys.* **2012**, *14*, 13292−13298.
(19) Blankenburg, S.; Bieri, M.; Fasel, R.; Mullen, K.; Pignedoli, C. A.; Passerone, D. Porous graphene as an atmospheric nanofilter. *Small* **2010**, *6*, 2266−2271.
(20) Fischbein, M.; Drndić, M. Electron beam nanosculpting of suspended graphene sheets. *Appl. Phys. Lett.* **2008**, *93*, No. 113107.
(21) Kuhn, P.; Forget, A.; Su, D. S.; Thomas, A.; Antonietti, M. From Microporous Regular Frameworks to Mesoporous Materials with Ultrahigh surface Area: Dynamic Reorganization of Porous Polymer Networks. *J. Am. Chem. Soc.* **2008**, *130*, 13333−13337.
(22) Koenig, S. P.; Wang, L.; Pellegrino, J.; Bunch, J. S. Selective molecular sieving through porous graphene. *Nat. Nanotechnol.* **2012**, *7*, 728−732.
(23) Li, Z.; Chen, F. Ion beam modification of two-dimensional materials: Characterization, properties, and applications. *Appl. Phys. Rev.* **2017**, *4*, No. 011103.
(24) Bai, Z.; Zhang, L.; Li, H.; Liu, L. Nanopore Creation in Graphene by Ion Beam Irradiation: Geometry, Quality, and Efficiency. *ACS Appl. Mater. Interfaces* **2016**, *8*, 24803−24809.
(25) Zhao, S.; Xue, J. Modification of graphene supported on SiO_2 substrate with swift heavy ions from atomistic simulation point. *Carbon* **2015**, *93*, 169−179.
(26) Li, W.; Wang, X.; Zhang, X.; Zhao, S.; Duan, H.; Xue, J. Mechanism of the defect formation in supported graphene by energetic heavy ion irradiation: the substrate effect. *Sci. Rep.* **2015**, *5*, No. 9935.
(27) Li, W.; Liang, L.; Zhao, S.; Zhang, S.; Xue, J. Fabrication of nanopores in a graphene sheet with heavy ions: A molecular dynamics study. *J. Appl. Phys.* **2013**, *114*, No. 234304.
(28) Zhao, S.; Xue, J.; Wang, Y.; Yan, S. Effect of SiO_2 substrate on the irradiation-assisted manipulation of supported graphene: a molecular dynamics study. *Nanotechnology* **2012**, *23*, No. 285703.
(29) Zhao, S.; Xue, J.; Liang, L.; Wang, Y.; Yan, S. Drilling Nanopores in Graphene with Clusters: A Molecular Dynamics Study. *J. Phys. Chem. C* **2012**, *116*, 11776−11782.
(30) Vázquez, H.; Ahlgren, E. H.; Ochedowski, O.; Leino, A. A.; Mirzayev, R.; Kozubek, R.; Lebius, H.; Karlusic, M.; Jaksic, M.; Krasheninnikov, A. V.; Kotakoski, J.; Schleberger, M.; Nordlund, K.; Djurabekova, F. Creating nanoporous graphene with swift heavy ions. *Carbon* **2017**, *119*, 200.
(31) O'Hern, S. C.; Boutilier, M. S.; Idrobo, J. C.; Song, Y.; Kong, J.; Laoui, T.; Atieh, M.; Karnik, R. Selective ionic transport through tunable subnanometer pores in single-layer graphene membranes. *Nano Lett.* **2014**, *14*, 1234−1241.
(32) Ghorbani-Asl, M.; Kretschmer, S.; Spearot, D. E.; Krasheninnikov, A. V. Two-dimensional MoS_2 under ion irradiation: from controlled defect production to electronic structure engineering. *2D Mater.* **2017**, *4*, No. 025078.
(33) Madauß, L.; Ochedowski, O.; Lebius, H.; Ban-d'Etat, B.; Naylor, C. H.; Johnson, A. T. C.; Kotakoski, J.; Schleberger, M. Defect engineering of single- and few-layer MoS_2 by swift heavy ion irradiation. *2D Mater.* **2017**, *4*, No. 015034.
(34) Guo, H.; Sun, Y.; Zhai, P.; Yao, H.; Zeng, J.; Zhang, S.; Duan, J.; Hou, M.; Khan, M.; Liu, J. Swift-heavy ion irradiation-induced latent tracks in few- and mono-layer MoS_2. *Appl. Phys. A* **2016**, *122*, No. 375.
(35) Kim, T. Y.; Cho, K.; Park, W.; Park, J.; Song, Y.; Hong, S.; Hong, W. K.; Lee, T. Irradiation effects of high-energy proton beams on MoS_2 field effect transistors. *ACS Nano* **2014**, *8*, 2774−2781.
(36) Ma, Q.; Odenthal, P. M.; Mann, J.; Le, D.; Wang, C. S.; Zhu, Y.; Chen, T.; Sun, D.; Yamaguchi, K.; Tran, T.; Wurch, M.; McKinley, J. L.; Wyrick, J.; Magnone, K.; Heinz, T. F.; Rahman, T. S.; Kawakami, R.; Bartels, L. Controlled argon beam-induced desulfurization of

DOI: 10.1021/acsami.8b10569
ACS Appl. Mater. Interfaces 2018, 10, 28909−28917

monolayer molybdenum disulfide. *J. Phys.: Condens. Matter* **2013**, *25*, No. 252201.
(37) Bai, Z.; Zhang, L.; Liu, L. Bombarding Graphene with Oxygen Ions: Combining Effects of Incident Angle and Ion Energy To Control Defect Generation. *J. Phys. Chem. C* **2015**, *119*, 26793−26802.
(38) Zhao, S.; Xue, J.; Kang, W. Ion selection of charge-modified large nanopores in a graphene sheet. *J. Chem. Phys.* **2013**, *139*, No. 114702.
(39) Khare, K. S.; Khare, R. Directed Diffusion Approach for Preparing Atomistic Models of Crosslinked Epoxy for Use in Molecular Simulations. *Macromol. Theory Simul.* **2012**, *21*, 322−327.
(40) Jiang, J.-W.; Park, H. S.; Rabczuk, T. Molecular dynamics simulations of single-layer molybdenum disulphide (MoS_2): Stillinger-Weber parametrization, mechanical properties, and thermal conductivity. *J. Appl. Phys.* **2013**, *114*, No. 064307.
(41) Jiang, J. W. Parametrization of Stillinger-Weber potential based on valence force field model: application to single-layer MoS_2 and black phosphorus. *Nanotechnology* **2015**, *26*, No. 315706.
(42) *The Stopping and Range of Ions in Solids*; Ziegler, J. F.; Biersack, J. P.; Littmark, U., Eds.; Pergamon: New York, 1985.
(43) Tersoff, J. New empirical approach for the structure and energy of covalent systems. *Phys. Rev. B* **1988**, *37*, 6991−7000.
(44) Hohenberg, P.; Kohn, W. Inhomogeneous Electron Gas. *Phys. Rev.* **1964**, *136*, B864−B871.
(45) Kresse, G.; Furthmüller, J. Efficiency of ab-initio total energy calculations for metals and semiconductors using a plane-wave basis set. *Comput. Mater. Sci.* **1996**, *6*, 15−50.
(46) Kresse, G.; Furthmüller, J. Efficient iterative schemes for ab initio total-energy calculations using a plane-wave basis set. *Phys. Rev. B* **1996**, *54*, 11169−11186.
(47) Blöchl, P. E. Projector augmented-wave method. *Phys. Rev. B* **1994**, *50*, 17953−17979.
(48) Kresse, G.; Joubert, D. From ultrasoft pseudopotentials to the projector augmented-wave method. *Phys. Rev. B* **1999**, *59*, 1758−1775.
(49) Perdew, J. P.; Burke, K.; Ernzerhof, M. Generalized Gradient Approximation Made Simple. *Phys. Rev. Lett.* **1996**, *77*, 3865−3868.
(50) Klimeš, J.; Bowler, D. R.; Michaelides, A. Chemical accuracy for the van der Waals density functional. *J. Phys.: Condens. Matter* **2010**, *22*, No. 022201.
(51) Guo, X.; Zhang, X.; Zhao, S.; Huang, Q.; Xue, J. High adsorption capacity of heavy metals on two-dimensional MXenes: an ab initio study with molecular dynamics simulation. *Phys. Chem. Chem. Phys.* **2016**, *18*, 228−233.
(52) Zhao, S.; Xue, J.; Kang, W. Gas adsorption on MoS_2 monolayer from first-principles calculations. *Chem. Phys. Lett.* **2014**, *595-596*, 35−42.
(53) Monkhorst, H. J.; Pack, J. D. Special points for Brillouin-zone integrations. *Phys. Rev. B* **1976**, *13*, 5188−5192.
(54) Henkelman, G.; Uberuaga, B. P.; Jonsson, H. A climbing image nudged elastic band method for finding saddle points and minimum energy paths. *J. Chem. Phys.* **2000**, *113*, 9901−9904.
(55) Lehtinen, O.; Kotakoski, J.; Krasheninnikov, A. V.; Tolvanen, A.; Nordlund, K.; Keinonen, J. Effects of ion bombardment on a two-dimensional target: Atomistic simulations of graphene irradiation. *Phys. Rev. B* **2010**, *81*, No. 153401.
(56) Krasheninnikov, A. V.; Nordlund, K.; Keinonen, J. Production of defects in supported carbon nanotubes under ion irradiation. *Phys. Rev. B* **2002**, *65*, No. 1654231.
(57) Pomoell, J. A. V.; Krasheninnikov, A. V.; Nordlund, K.; Keinonen, J. Ion ranges and irradiation-induced defects in multiwalled carbon nanotubes. *J. Appl. Phys.* **2004**, *96*, 2864−2871.
(58) Tolvanen, A.; Kotakoski, J.; Krasheninnikov, A. V.; Nordlund, K. Relative abundance of single and double vacancies in irradiated single-walled carbon nanotubes. *Appl. Phys. Lett.* **2007**, *91*, No. 173109.
(59) Ziegler, J. F.; Ziegler, M. D.; Biersack, J. P. SRIM − The stopping and range of ions in matter (2010). *Nucl. Instrum. Methods Phys. Res., Sect. B* **2010**, *268*, 1818−1823.
(60) Schleberger, M.; Lebius, H.; Akcöltekin, S.; Osmani, O.; Bukowska, H.; Peters, T.; Alzaher, I.; Monnet, I.; d'Etat, B. Unzipping and folding of graphene by swift heavy ions. *Appl. Phys. Lett.* **2011**, *98*, No. 103103.
(61) Muszynski, R.; Seger, B.; Kamat, P. V. Decorating graphene sheets with gold nanoparticles. *J. Phys. Chem. C* **2008**, *112*, 5263−5266.
(62) Gruber, E.; Wilhelm, R. A.; Petuya, R.; Smejkal, V.; Kozubek, R.; Hierzenberger, A.; Bayer, B. C.; Aldazabal, I.; Kazansky, A. K.; Libisch, F.; Krasheninnikov, A. V.; Schleberger, M.; Facsko, S.; Borisov, A. G.; Arnau, A.; Aumayr, F. Ultrafast electronic response of graphene to a strong and localized electric field. *Nat. Commun.* **2016**, *7*, No. 13948.
(63) Hu, W.; Wu, X.; Li, Z.; Yang, J. Helium separation via porous silicene based ultimate membrane. *Nanoscale* **2013**, *5*, 9062−9066.
(64) Tsuru, T.; Igi, R.; Kanezashi, M.; Yoshioka, T.; Fujisaki, S.; iwamoto, Y. Permeation properties of hydrogen and water vapor through porous silica membranes at high temperatures. *AIChE J.* **2011**, *57*, 618−629.
(65) Kanezashi, M.; Yada, K.; Yoshioka, T.; Tsuru, T. Organic−inorganic hybrid silica membranes with controlled silica network size: Preparation and gas permeation characteristics. *J. Membr. Sci.* **2010**, *348*, 310−318.
(66) Mehio, N.; Dai, S.; Jiang, D. E. Quantum Mechanical Basis for Kinetic Diameters of Small Gaseous Molecules. *J. Phys. Chem. A* **2014**, *118*, 1150−1154.
(67) Breck, D. W. *Zeolite Molecular Sieves: Structure, Chemistry, and Use*; Wiley: New York, 1974.
(68) Bampoulis, P.; van Bremen, R.; Yao, Q.; Poelsema, B.; Zandvliet, H. J. W.; Sotthewes, K. Defect Dominated Charge Transport and Fermi Level Pinning in MoS_2/Metal Contacts. *ACS Appl. Mater. Interfaces* **2017**, *9*, 19278−19286.
(69) Ghorbani-Asl, M.; Enyashin, A. N.; Kuc, A.; Seifert, G.; Heine, T. Defect-induced conductivity anisotropy in MoS_2 monolayers. *Phys. Rev. B* **2013**, *88*, No. 245440.
(70) Park, J. H.; Sanne, A.; Guo, Y. Z.; Amani, M.; Zhang, K. H.; Movva, H. C. P.; Robinson, J. A.; Javey, A.; Robertson, J.; Banerjee, S. K.; Kummel, A. C. Defect passivation of transition metal dichalcogenides via a charge transfer van der Waals interface. *Sci. Adv.* **2017**, *3*, No. e1701661.
(71) Tang, W.; Sanville, E.; Henkelman, G. A grid-based Bader analysis algorithm without lattice bias. *J. Phys.: Condens. Matter* **2009**, *21*, No. 084204.

DOI: 10.1021/acsami.8b10569
ACS Appl. Mater. Interfaces 2018, 10, 28909−28917